Geomorphology 153–154 (2012) 39–47

Contents lists available at SciVerse ScienceDirect

Geomorphology

journal homepage: www.elsevier.com/locate/geomorph

# Inception of bed load motion beneath a bore

Nazanin Khezri, Hubert Chanson *

*The University of Queensland, School of Civil Engineering, Brisbane QLD 4072, Australia*

ARTICLE INFO

*Article history:*
Received 5 December 2011
Received in revised form 5 February 2012
Accepted 9 February 2012
Available online 17 February 2012

*Keywords:*
Tidal bores
Bed load motion
Inception
Longitudinal pressure gradient
Forces

ABSTRACT

A tidal bore is a series of waves propagating upstream in the river mouth as the tidal flow turns to rising in macro-tidal conditions. Some related geophysical processes include the tsunami-induced bores and uprushing bores on beaches. In the present study, the inception of sediment motion beneath tidal bores was investigated physically. No sediment motion was observed in the initially steady flow and beneath undular bores. A transient sheet flow motion was observed beneath breaking bores and the onset of sediment motion was closely linked with the passage of the roller toe. The forces acting on the movable gravel bed particles were estimated from the physical measurements. The results showed that the longitudinal pressure gradient force was the dominant contribution de-stabilising the particles and inducing the onset of sediment motion. The drag force added a sizeable contribution to maintain the upstream particle motion, although the entire sheet flow motion was brief.



## 1. Introduction

A tidal bore is a series of waves propagating upstream in the river mouth as the tidal flow turns to rising (Fig. 1A, B). The bore occurs during the flood tide under appropriate tidal, bathymetric and riverine conditions (Tricker, 1965; Chanson, 2011). Some related geophysical processes include the tsunami-induced bores when a tsunami wave propagating in shallow-water regions is led by a bore and the swash-induced bores on beaches when the wave runup encounters some rundown (Fig. 1C). The propagation of bores is known to play a major role in terms of sedimentary motion (Chen et al., 1990; Tessier and Terwindt, 1994; Chanson et al., 2011), although the dominant driving mechanism of sediment motion inception remains unclear.

In steady flows, a number of studies used photographic and video techniques to investigate the bed load motion (Sumer and Oguz, 1978; Nino and Garcia, 1998). Despite a few studies in gradually varied flows (Bombar et al., 2011), no systematic study was performed in highly unsteady open channel flows. In such rapidly-varied flows, the large scale vortices may play an important role in terms of sediment pickup and, when the turbulent mixing length is much larger than the sediment distribution length scale, the validity of the Shields diagram application is arguable (Nielsen, 1992). The present study examines the propagation of tidal bores with a focus on the mechanisms of sediment transport inception. The analysis is based upon a physical study based upon a Froude dynamic similarity performed on a movable gravel bed. The results based upon individual particle motion show the relative significance of longitudinal pressure gradient and drag forces beneath the bore. It is the aim of this work to characterise the seminal features of bed load motion inception beneath tidal bores and to provide quantitative details such as particle velocities and accelerations to improve future sediment transport models.

### 1.1. Theoretical considerations

In unsteady open channel flow phenomena such as a bore propagating over movable beds (Fig. 2), the forces acting on each sediment particle include the gravity force, the buoyancy force, the shear/drag force, the lift force, the resultant of the reaction forces of the surrounding grains (or intergranular force), the longitudinal pressure gradient, the Magnus force, the virtual mass force and the Basset history force. The buoyancy and gravity forces act along the vertical, the drag force along the flow direction and the lift force in the direction perpendicular to the flow (Fig. 2). For a submerged sediment particle on the horizontal channel bed, Newton's law of motion applied to the particle in the longitudinal direction yields in first approximation:

$$m_s \frac{\partial V_s}{\partial t} = F_{drag} + F_p + F_{virtual} + \left(F_{grain}\right)_x + F_{Basset} \quad (1)$$

where $m_s$ is the particle mass, $V_s$ is the horizontal particle velocity component and the forces acting on the particle initially at rest are the drag force $F_{drag}$, a longitudinal pressure gradient force $F_p$, a virtual mass force $F_{virtual}$, the intergranular force component in the horizontal direction $(F_{grain})_x$ and the Basset history force. Since this study is concerned with the onset of sediment motion,

* Corresponding author. Tel.: +61 7 3365 4163; fax: +61 7 3365 4599.
*E-mail address:* h.chanson@uq.edu.au (H. Chanson).

0169-555X/$ – see front matter © 2012 Elsevier B.V. All rights reserved.
doi:10.1016/j.geomorph.2012.02.006

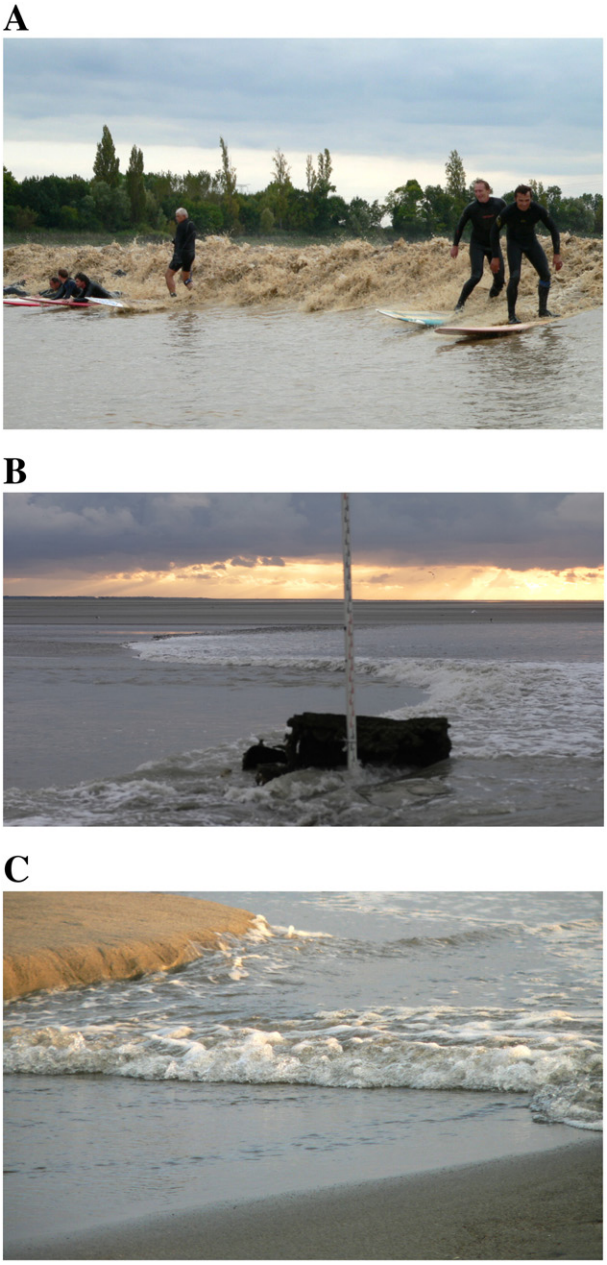


**Fig. 1.** Photographs of bores — bore propagation from right to left. (A) Tidal bore of the Dordogne River at Asques (France) on 30 September 2008 afternoon, U~2 m/s. (B) Tidal bore of the Sélune River at Vains (France) on 24 September 2010, $d_o$ = 0.38 m, U = 2.0 m/s, Fr = 2.35. (C) Swash-induced bore in a small inlet at Ikobe Beach, Enshu coast (Japan) on 14 November 2008, $d_o$~0.05 m, U~0.5 m/s.

the particle is initially at rest and the Basset history term will be assumed small in the following paragraphs, while the intergranular force is commonly unknown.

For a particle in motion, the drag force is:

$$F_{drag} = \frac{1}{2} C_d \rho (V_x - V_s)|V_x - V_s| A_s \quad (2)$$

where $C_d$ is the drag coefficient, $\rho$ is the water density, $V_x$ is the longitudinal water velocity component positive downstream, $|V_x|$ is the velocity component magnitude, $A_s$ is the projected area of the sediment particle, and the particle velocity $V_s$ is positive downstream.

In presence of a longitudinal pressure gradient $\partial P/\partial x$ as beneath a tidal bore (Fig. 2), the longitudinal pressure force on a fixed particle is:

$$F_p = -\frac{\partial P}{\partial x} A_s h_s \quad (3a)$$

where P is the pressure, $h_s$ is a characteristic particle dimension and x is the longitudinal direction positive downstream (Fig. 2). For a spherical particle with diameter $d_s$, the longitudinal pressure gradient force equals:

$$F_p = -\frac{\partial P}{\partial x} \frac{\pi}{6} d_s^3 \quad (3b)$$

In Eq. (3), the longitudinal pressure gradient $\partial P/\partial x$ is assumed constant across the particle, an assumption which might not be accurate for large particles beneath to the roller toe.

The virtual mass force is:

$$F_{virtual} = \frac{m_s}{s} C_m \frac{\partial (V - V_s)}{\partial t} \quad (4)$$

where s is the particle relative density and $C_m$ is an added mass coefficient function of the particle shape and flow conditions (Brennen, 1982).

## 2. Experimental apparatus and methods

### 2.1. Experimental facility

The inception of sediment motion beneath a bore was investigated physically in a relatively large flume at the University of Queensland (Figs. 3 and 4). The test section was 12 m long and 0.5 m wide with a PVC bed and glass side walls. The waters were supplied by a constant head reservoir feeding into a large intake, 2.1 m long, 1.1 m wide and 1.1 m deep, leading to the test section through a smooth convergent. At the channel downstream end (x = 11.15 m), where x is the distance from the channel upstream end, a fast-closing tainter gate was installed.

The water discharge was measured with two orifice meters designed based upon the British Standards (British Standard, 1943) and calibrated on site with a volume per time method. The percentage of error was estimated to be less than 2%. In steady flows, the water depths were measured using rail mounted pointer gauges. The unsteady water depths were recorded with a series of acoustic displacement meters. A Microsonic™ Mic + 35/IU/TC unit was located at x = 10.8 m, where x is the longitudinal distance from the test section upstream end. Three acoustic displacement meters Microsonic™ Mic + 25/IU/TC were installed above the channel at x = 4, 5 and 6 m. The acoustic displacement meters were calibrated against the pointer gauges in steady flows.

The velocity measurements were performed using an acoustic Doppler velocimeter Nortek™ Vectrino + (Serial No. VNO 0436) equipped with a three-dimensional side-looking head (Fig. 3). The velocity range was 1.0 m/s and the sampling rate was 200 Hz. The data accuracy was 1% of the velocity range. Both the acoustic displacement meters and acoustic Doppler velocimeter were synchronised within +/−1 ms. The translation of the ADV probe in the vertical direction was controlled by a fine adjustment travelling mechanism connected to a Mitutoyo™ digimatic scale unit, with an error on the vertical position of less than 0.025 mm. The accuracy on the longitudinal position was estimated as $\Delta x < \pm 2$ mm. All the measurements were taken on the channel centreline. The post-processing of the ADV signal was limited to a removal of communication errors, although the vertical velocity component $V_z$ data might be affected adversely by the bed proximity for z < 0.030 m.

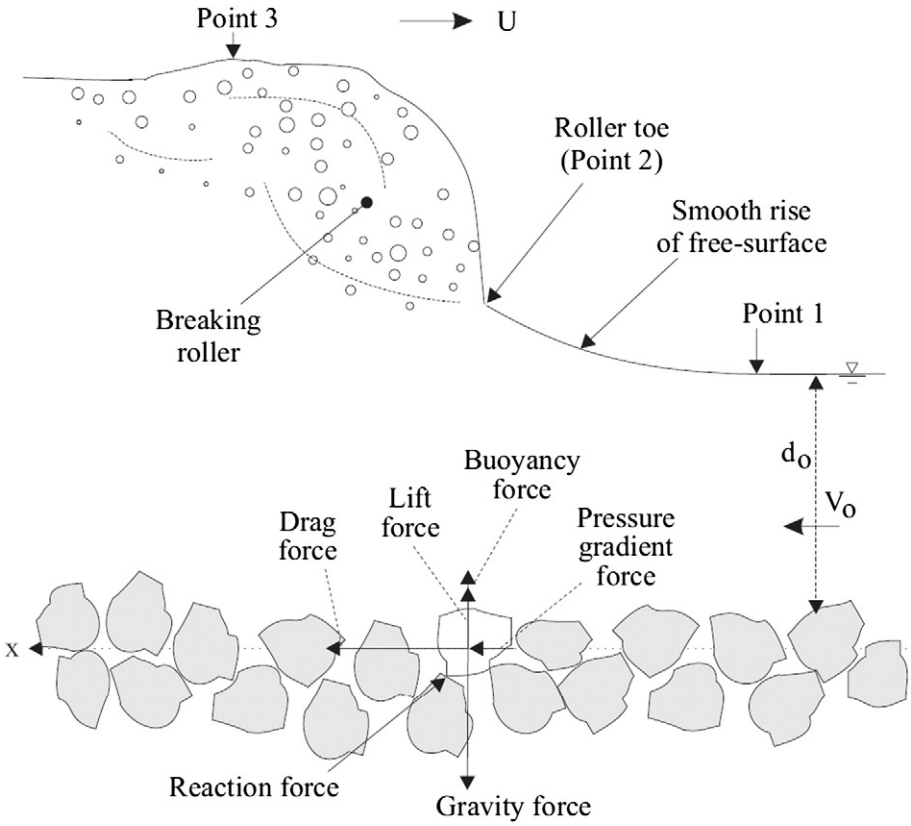


**Fig. 2.** Sketch of the major forces acting on a sediment particle beneath a bore.

### 2.2. Bed material and particle tracking

For all experiments, the PVC bed was covered with a series of plywood sheets, 1.2 m long and 0.5 m wide, covered by natural blue granite gravels (relative density, $s = 2.65$) which were sieved between 4.75 mm and 6.70 mm, glued in resin and covered by a spray gloss surface finish. Between $x = 4.5$ and 5.5 m, a 1 m long section of smooth-painted plywood sheet was covered by a layer of loose gravels, spread evenly prior to each experimental run. The mobile bed layer was about 2–3 grain diameters thick.

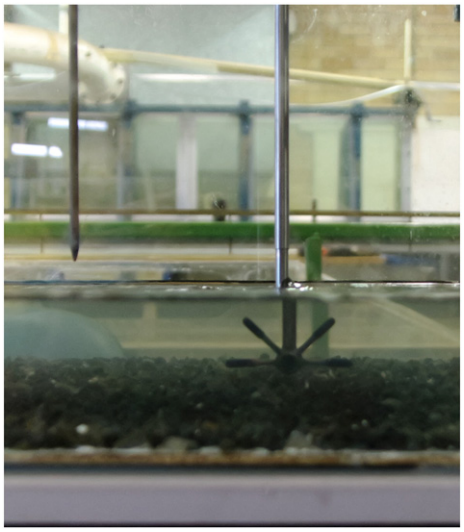

**Fig. 3.** Acoustic Doppler velocimeter (ADV) in the initially steady flow above the gravel bed — Pointer gauge (left) above the free-surface and ADV head (right) — flow from right to left.

The water depth was measured above the top of the gravel bed using a semi-circular footing with a 25.1 $cm^2$ area. The hydraulic roughness of gravel bed was tested in steady flows with Reynolds numbers ranging from $2.4 \times 10^4$ to $5.6 \times 10^5$, yielding on average a Darcy-Weisbach friction factor $f = 0.036$ corresponding to an equivalent sand roughness height of 3.4 mm, comparable to the typical gravel size $d_s = 5.7$ mm.

The sediment particle motion was studied using a digital video-camera Panasonic™ NV-GC300 (25 fps). More than 25 video movies were made for each Froude number and at least 15 to 20 painted particles were tracked on average per video. The total number of particles in motion was much larger for each movie, but only particles within the depth of field of the camera lens were followed. Additional information was obtained with a dSLR Pentax™ K-7 camera.

### 2.3. Tidal bore generation

The tidal bore was generated by the rapid partial closure of a downstream tainter gate located at $x = 11.15$ m. The gate was similar to that used by Koch and Chanson (2009) and Chanson (2010). The closure time was between 0.1 and 0.15 s. Lubin et al. (2010) presented a computational modelling of the gate closure process.

The experimental flow conditions were selected to generate both undular bores and breaking surges using the same initial flow rate Q. The main dependent parameter was downstream gate opening after closure. The initially steady flow conditions were established for at least 5 minutes prior to the measurements and the data acquisition was started 60 s before gate closure. After gate closure, the bore propagated upstream and each experiment was stopped before the bore front reached the upstream intake structure. While a number of flow conditions were tested, detailed velocity and sediment motion measurements were conducted for two Froude numbers and the experimental flow conditions are summarised in Table 1. The velocity

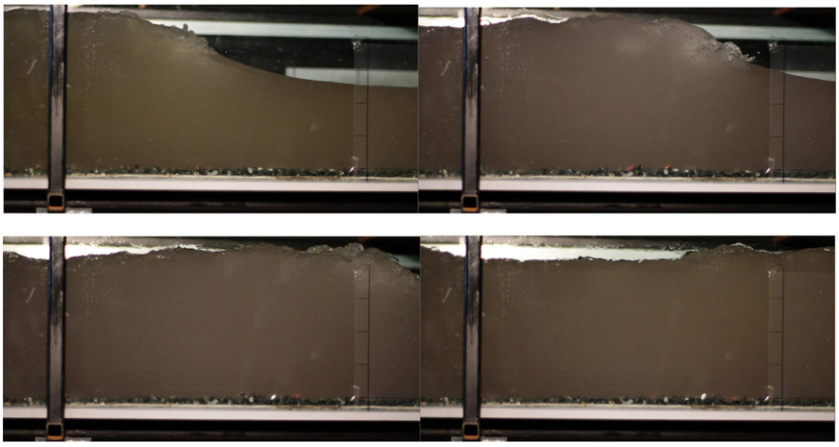

**Fig. 4.** Breaking bore propagating upstream on movable gravel bed (Fr = 1.4, Q = 0.051 $m^3/s$, $d_o$ = 0.136 m, shutter speed: 1/1000 s) — bore propagation from left to right — from left to right, top to bottom, $t = t_o$, $t_o + 0.19$ s, $t_o + 0.38$ s, $t_o + 0.58$ s.

measurements were performed at x = 5 m, and the particle tracking by video were conducted between x = 4.5 and 5.5 m.

## 3. Results

### 3.1. General observations

A number of observations were conducted with bore Froude numbers between 1 and 1.45, where the Froude number is defined as:

$$Fr = \frac{V_o + U}{\sqrt{g\ d_o}} \quad (5)$$

with $d_o$ the initial flow depth, $V_o$ the initial flow velocity positive downstream, g the acceleration due to gravity and U the surge front celerity positive upstream (Fig. 2). The results showed the occurrence of an undular bore for Froude numbers between 1 and 1.3, and a breaking bore with a marked roller was observed for Fr > 1.3 to 1.4. Fig. 4 shows four photographs taken rapidly, within 0.6 s, of a breaking bore propagating over the movable gravel bed. Two movies are also included as part of the video data (Table 2).

No sediment motion was observed in the initially steady flow. Beneath the undular bores, the sediment movement was negligible. No more than one to two particles would move a very short distance, mostly as incomplete rotation of the particle rather a position change. For example, during the run shown in the movie 531-run13-S60.avi, no sediment motion is observed. During the breaking tidal bores, a large number of particles were set into motion and moved upstream behind the bore. For example, see the movie 531-run14-S0.avi. The inception of gravel motion was associated mostly, although not always, with the passage of the roller toe (Point 2, Fig. 2) as shown in Fig. 5. Fig. 5A presents a picture taken immediately prior to the roller toe passage and Fig. 5B shows the trajectories of a number of selected particles labelled from A to O in Fig. 5A. (In Fig. 5B, X is positive upstream.) The particle trajectories are compared with three characteristic features of the roller toe: Point 1 where the free-surface started to curved upwards ahead of the roller, Point 2 which was the roller toe and Point 3 which corresponded to the roller maximum elevation (Fig. 2). These three locations are sketched in Fig. 2 and the complete data set is shown in Fig. 6 in a dimensionless form.

The velocity data for both breaking and undular bores indicated a rapid flow deceleration during the bore passage (Fig. 7). Please note that the vertical scale differs between Figs. 7A and B. Beneath the breaking bore, the longitudinal velocity data highlighted a transient recirculation next to the bed as illustrated in Fig. 7B. Such a transient recirculation was previously reported by Koch and Chanson (2009) and Chanson (2010), and it is believed to be a characteristic feature of breaking bore. Fig. 7 presents some typical time-variations of the water depth d and longitudinal velocity component $V_x$, where $V_x$ is positive downstream. In Fig. 7B, the transient recirculation is seen for $610 < t(g/d_o)^{1/2} < 640$.

### 3.2. Gravel particle motion beneath a breaking bore

Strong sediment motion was observed beneath the breaking bore (see video data 531-run14-S0.avi). A significant number of gravel bed particles were set into motion by the bore passage in the form of a transient sheet flow. The data implied that the sediment inception was mainly linked with the passage of the roller toe (Point 2, Fig. 2). Once entrained, the particles presented a number of patterns. Some particles were entrained rapidly: e.g., particles A, D, E, M, O in Fig. 5B. Others were transported more slowly, for example particles B, H, I in Fig. 5B, while some were entrained initially rapidly and continued more slowly: e.g., particles C, K in Fig. 5B. The range of particle behaviour was broad, from some particles with almost no movement to a few saltating particles which were subjected to a high initial acceleration, sometimes even as much as twice the gravity acceleration. The properties of the gravel motion were recorded in terms of the maximum and mean gravel particle velocities, their maximum acceleration and travel duration. The statistical characteristics are summarised in Fig. 8 for the breaking bore experiment listed in Table 1.

The maximum accelerations of the particles during the passage of the bore are presented in Fig. 8A and B. More than half of the particles experienced a maximum acceleration greater than 0.4 g and about 10% of particles reached a maximum horizontal acceleration greater

**Table 1**
Experimental investigations of tidal bore propagation on movable bed.

| Bed configuration | Gate opening (mm) | Q ($m^3/s$) | $d_o$ (m) | $V_o$ (m/s) | U (m/s) | Fr | Bore type | $d_{conj}/d_o$ | Instrument |
|---|---|---|---|---|---|---|---|---|---|
| Mobile Bed | 0 | 0.051 | 0.136 | 0.75 | 0.87 | 1.40 | Breaking | 1.64 | ADV (x = 5 m) & Particle tracking (4.5 < x < 5.5 m) |
| | 60 | 0.050 | 0.136 | 0.74 | 0.61 | 1.17 | Undular | 1.30 | |

Notes: $d_o$: initial flow depth; $d_{conj}$: conjugate flow depth; Fr: bore Froude number; Q: initial flow rate; U: bore celerity; $V_o$: initial flow velocity.

**Table 2**
Video files: tidal bore propagation above movable gravel bed.

| Filename | Bore type | Bed | Flow conditions | Description |
|---|---|---|---|---|
| 531-run14-S0.avi | Breaking | Mobile bed | Fr = 1.4, Q = 0.051 $m^3/s$, $d_o$ = 0.136 m, U = 0.87 m/s | Breaking bore propagation above mobile gravel bed |
| 531-run13-S60.avi | Undular | Mobile bed | Fr = 1.17, Q = 0.050 $m^3/s$, $d_o$ = 0.136 m, U = 0.61 m/s | Undular bore propagation above mobile gravel bed |

than 1 g, where g is the gravity acceleration. The maximum accelerations were found to occur mostly immediately after the bore toe ($t-T_2>0$) with $t=T_2$ corresponding to the roller toe passage (Point 2) (Fig. 8A).

The particle average and maximum velocities during the passage of the bore are also presented in Fig. 8C and D as histograms. The particle velocities were about $\overline{V_s}/U \approx -0.14$ on average while the maximum particles velocities reached value up to $(V_s)_{max}/U \approx -0.69$, where U is the bore celerity (Table 1) and the negative sign reflect the upstream advection of the sediments. Note that the particle velocities were comparable to the transient fluid velocity data observed close to the bed: e.g., $V_x/U \approx -0.08$ to $-0.6$ ($V_x/V_o \approx -0.1$ to $-0.7$) at $z/d_o = 0.09$ in Fig. 7B. The data in terms of duration of particle motion during the bore passage are presented in Fig. 8E. The particle motion was brief, with about 50% of particle moving for less than 0.3 s.

## 4. Application

The forces acting on the bed sediment particles were estimated based upon the free-surface properties, the velocity measurements next to the bed and the particle velocity data. For each tracked particle, the physical data provided the net force ($F = m_s a$) acting on each particle, where $a = \partial V_s/\partial x$ is the particle acceleration, while the longitudinal pressure gradient, virtual mass and shear forces were calculated. The longitudinal pressure gradient during the bore passage was deduced from the bore free-surface profile assuming hydrostatic pressure distributions. (Note that the Boussinesq equation was tested to calculate the non-hydrostatic pressure field upstream of the roller toe based upon the free-surface curvature; the results showed less than 5% difference from the hydrostatic pressure calculations.) The pressure gradient force is presented in Fig. 9. In the initially steady flow, the longitudinal pressure force was zero, while the pressure gradient tended to an infinite value at the roller toe (Point 2). The drag force acting on a particle was estimated using Eq. (2), assuming spherical particles. The mean longitudinal velocity component at $z/d_o = 0.06$ was used to estimate the longitudinal fluid velocity, while the particle velocity was deduced from the particle tracking trajectories. Herein the mean velocity was the low-pass filtered velocity signal (cutoff frequency: 2 Hz) shown in Fig. 7. Similarly the virtual mass force was calculated using Eq. (4) assuming a spherical particle ($C_m = 0.5$). The results are summarised in Fig. 9 for more than 200 particles, where $T_2$ is the time when the particle is exactly beneath the roller toe (Point 2), and $t-T_2=0$ corresponds to the instant when the bore toe passed immediately above the gravel particle.

A number of trends were observed. Many particles reached their highest acceleration when the longitudinal pressure gradient force amplitude was maximum, although some started to move shortly before or after the roller toe passage. The finding is consistent with the results of Madsen (1974), although his development was based upon geotechnical considerations for a sandy material beneath breaking waves. The longitudinal pressure gradient force had the largest impact on the onset of particle motion, while the virtual mass force

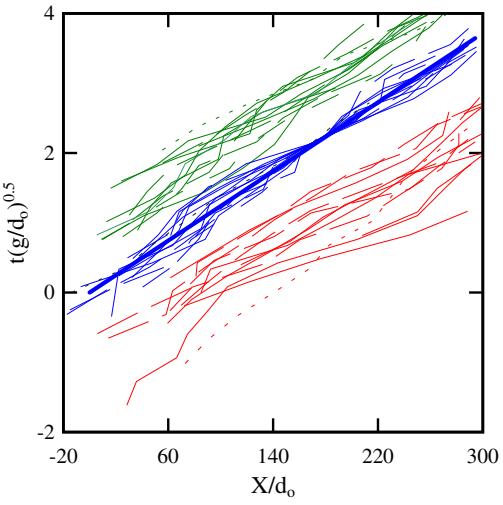


**Fig. 6.** Characteristic points of the breaking bore free-surface (Fr = 1.4, Q = 0.051 $m^3/s$, $d_o$ = 0.136 m) — bore propagation from left to right.

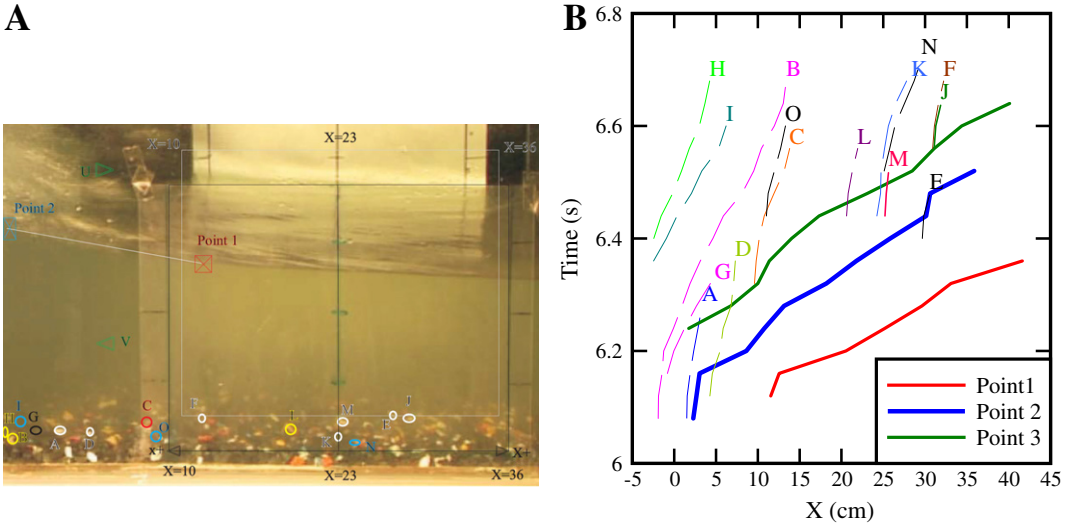


**Fig. 5.** Bed load motion during a single a breaking bore event (Fr = 1.4, Q = 0.051 $m^3/s$, $d_o$ = 0.136 m, run 32) — bore propagation from left to right. (A, Left) Photograph of the incoming bore propagating from left to right. (B, Right) Gravel particle trajectories.

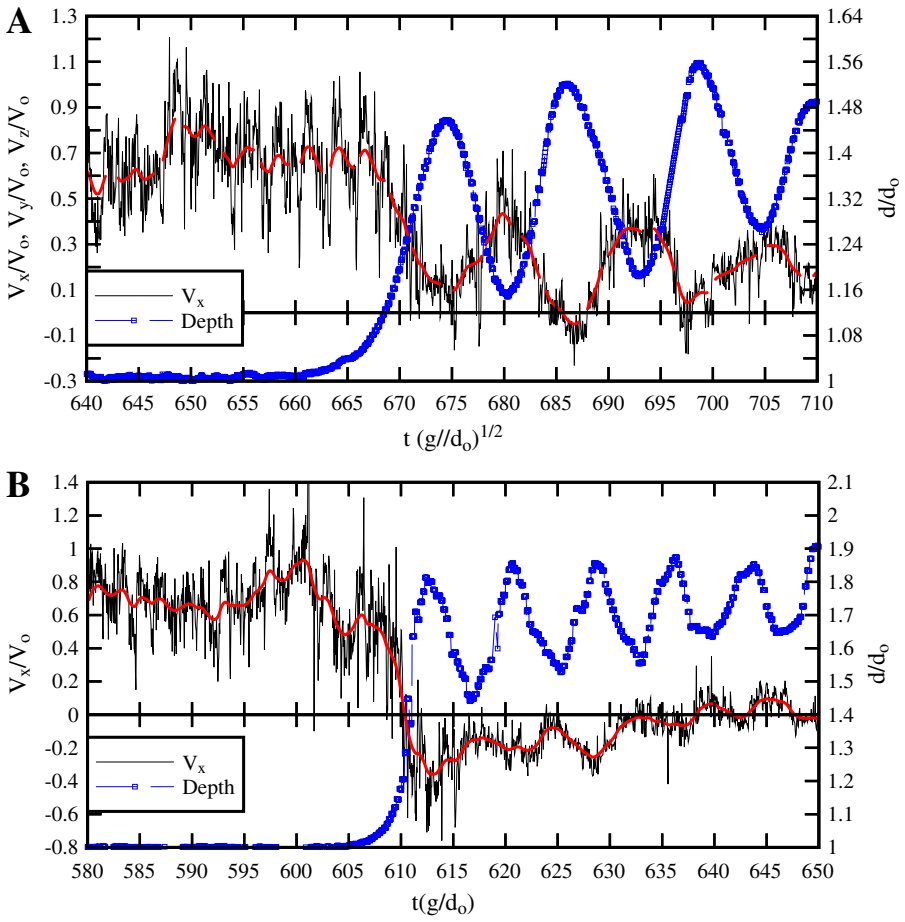


**Fig. 7.** Instantaneous water depth and longitudinal velocity beneath a tidal bore close to the mobile bed. (A) Undular bore experiment: Fr = 1.17, Q = 0.050 m$^3$/s, $d_o$ = 0.136 m, z/$d_o$ = 0.09. (B) Breaking bore experiment: Fr = 1.4, Q = 0.051 m$^3$/s, $d_o$ = 0.136 m, z/$d_o$ = 0.09.

had the least effect. The shear force acting on the particle decreased dramatically with the bore arrival; with increasing time when the pressure gradient decreased, the effect of drag force on the particle motion increased. The combination of the pressure gradient and drag forces contributed mostly to the upstream particle motion. The particle stopped when neither longitudinal pressure gradient nor drag forces acted upstream on the particle.

The forces acting on the particles were ensemble-averaged to find the main trends, and the trend lines are shown in Fig. 9. The experimental data implied that the drag force acted on the majority of particles as shown in Fig. 9A for 95% of the particles, with a decrease in shear force with the bore arrival and a negative drag force after the roller toe passed above the particles. For the remainder (5%) of particles, a larger positive drag force was experienced. Note that the scales for Fig. 9A and B are identical. Fig. 9C shows the virtual mass forces acting on particles upstream and downstream of the bore toe. The experimental results suggested a small contribution of the virtual mass force compared to both the pressure gradient force and drag force. Fig. 9D presents the net forces acting on the particle ($F = m_s a$). The data were estimated from the measured accelerations of particles and corresponded to the resultant of all external forces acting on a particle (Eq. (1)). The results implied that, next to the onset of sediment motion, the pressure force was close to the net resultant force, despite some scatter (Fig. 9D). The finding suggested the predominance of pressure gradient force in terms of the inception of sediment motion.

The resultant of longitudinal pressure gradient, drag and virtual mass forces was compared with the net forces acting on the particle ($F = m_s a$). The results (not shown) indicated a close agreement between the resultant and net forces, but immediately after the roller toe passage for $0 < (t - T_2)(g/d_o)^{0.5} < 1$. During that time, the force budget implied a non-negligible contribution of other forces, including the intergranular force component.

## 5. Discussion

Overall, the present results highlighted some key findings. During the initially steady flow, no sediment motion was observed and the drag force fluctuated around a mean value about equal to the particle interaction force in absence of particle motion. When the bore arrived, the drag force decreased with the sudden decrease in velocity and, during the transient recirculation, the local flow reversal induced a shear force acting on the particle in negative direction (i.e. upstream). The longitudinal pressure gradient force caused by the sudden change in free surface profile was the predominant force during the inception stages of particle motion. Behind the bore, the negative drag force had a significant role to maintain the particle motion and hence on its extent. Yet the negative shear force did not last long and the particle motion ended after some time.

The study demonstrated the role of tidal bores in scouring the river bed material and contributing to upstream sediment motion. The findings were consistent with the field observations of Tessier and Terwindt (1994) who attributed the deformation of non-consolidated sediments to the passage of a tidal bore in the internal estuarine zone of the Mont Saint Michel Bay. Chanson (2011, pp. 123–124) reported the formation of a new river channel cut by the Sélune River tidal bore during a single event in 2008. The present data provide some quantitative data in terms of sediment onset,

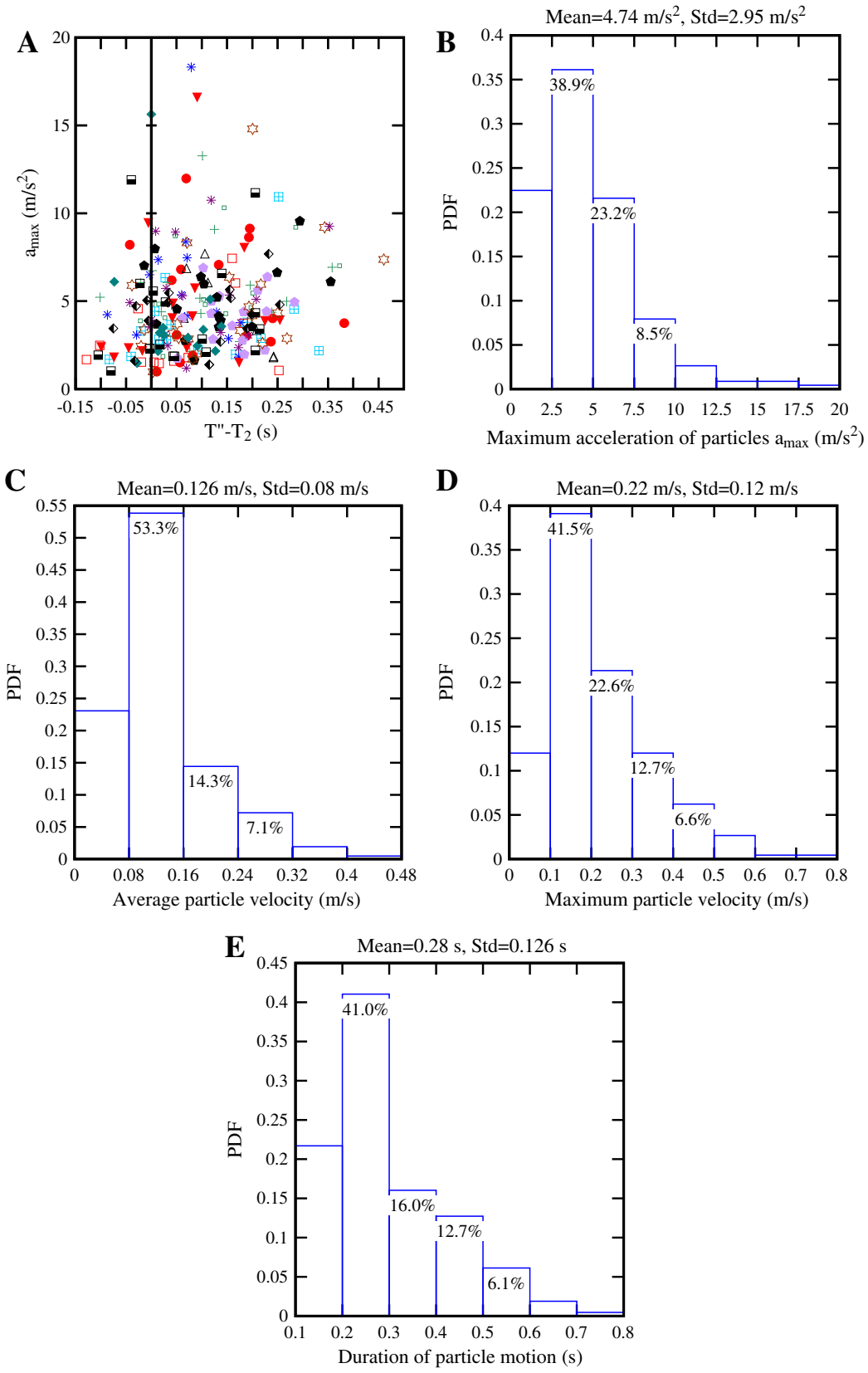


**Fig. 8.** Characteristics of gravel particle motion beneath a breaking bore (Fr = 1.4, Q = 0.051 $m^3/s$, $d_o$ = 0.136 m). (A, Left) Maximum particle acceleration beneath the breaking bore as function of the time of occurrence. (B, Right) Histogram of maximum particle accelerations. (C, Left) Histogram of average particle velocity. (D, Right) Histogram of maximum particle velocity. (E) Histogram of particle motion duration.

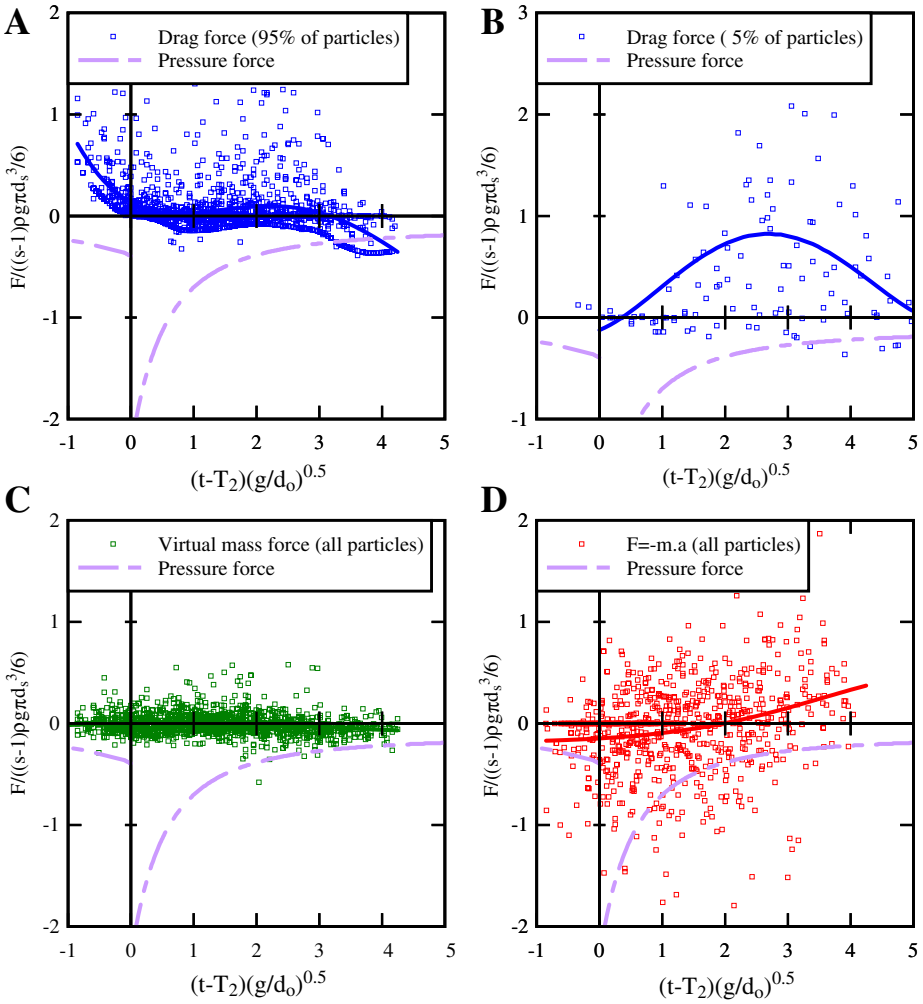


**Fig. 9.** Time-variations of forces acting on individual gravel particle beneath a breaking bore (Fr = 1.4, Q = 0.051 $m^3/s$, $d_o$ = 0.136 m). (A, Left) Dimensionless drag force for 95% of particles and longitudinal pressure gradient force. (B, Right) Dimensionless drag force for 5% of particles and longitudinal pressure gradient force. (C, Left) Dimensionless virtual mass force acting on particles and longitudinal pressure gradient force. (D, Right) Dimensionless net force acting on particles beneath a breaking bore.

particle acceleration and velocity beneath a bore which may explain the massive channel incision event.

## 6. Conclusion

The inception of sediment motion beneath bores was investigated physically with a range of complementary instrumentation. No sediment motion was observed in the initially steady flow and beneath the undular bores. Some transient sheet flow motion was observed beneath the breaking bores, and the onset of sediment motion was closely linked with the passage of the roller toe, characterised by some discontinuity of the free-surface slope.

During the physical experiments, the free-surface properties, and fluid and sediment velocities, were recorded. The particles were subjected to maximum accelerations of about 0.4 g on average, although a few particles were accelerated by more than 1.5 g. The particles were advected upstream with an average velocity $\overline{V_s}/U \approx -0.135$, while some particles reached a maximum velocity up to $(V_s)_{max}/U \approx -0.69$, where U is the bore celerity. The important forces acting on the movable gravel bed particles were estimated from the physical measurements. The results showed that the longitudinal pressure gradient force was the dominant contribution, de-stabilising the particles and inducing the sediment transport inception. The drag force added a significant effect to maintain the upstream particle motion, although the entire sheet flow motion was brief.

The propagation of tidal bores and uprushing bores on beaches has a significant impact in terms of the sediment process. The present study included geometric and kinematic sediment properties under this highly unsteady flow motion to assist future sediment transport models. Future physical contributions should yield further details into the flow physics with other particle characteristics including different granulometry and sediment density.

The manuscript is supplemented by two video movies taken with the digital video-camera Panasonic™ NV-GC300 (25 fps) (Table 2). The video frame was centered at x = 5 m. In each video movie, the first moments show the initially steady flow, with water flowing from right to left. The tidal bore generated at the channel downstream end propagates upstream (from left to right). During the undular bore movie (531-run13-S60.avi), no sediment motion is observed. On the other hand, a transient sheet flow is seen beneath the breaking bore (movie 531-run14-S0.avi). Supplementary materials related to this article can be found online at doi:10.1016/j.geomorph.2012.02.006.

## Acknowledgements

The authors acknowledge the technical assistance of Graham Illidge and Ahmed Ibrahim (The University of Queensland). They thank Dr Pierre Lubin (University of Bordeaux, France) for his helpful comments.

## References

Bombar, G., Elci, S., Tayfur, G., Guney, M.S., Bor, A., 2011. Experimental and numerical investigations of bed-load transport under unsteady flows. Journal of Hydraulic Engineering, ASCE 137, 1276–1282.

Brennen, C.E., 1982. A review of added mass and fluid inertial forces. Report CR82.010, Naval Civil Eng. Lab., Dept of Navy, Port Hueneme CA, USA.

British Standard, 1943. Flow measurement. British Standard Code BS 1042:1943. British Standard Institution, London.

Chanson, H., 2010. Unsteady turbulence in tidal bores: effects of bed roughness. Journal of Waterway, Port, Coastal, and Ocean Engineering, ASCE 136, 247–256. doi:10.1061/(ASCE)WW.1943-5460.0000048.

Chanson, H., 2011. Tidal Bores, Aegir, Eagre, Mascaret, Pororoca: Theory and Observations. World Scientific, Singapore.

Chanson, H., Reungoat, D., Simon, B., Lubin, P., 2011. High-frequency turbulence and suspended sediment concentration measurements in the garonne river tidal bore. Estuarine, Coastal and Shelf Science 95, 298–306. doi:10.1016/j.ecss.2011.09.012.

Chen, J., Liu, C., Zhang, C., Walker, H.J., 1990. Geomorphological development and sedimentation in qiantang estuary and hangzhou bay. Journal of Coastal Research 6, 559–572.

Koch, C., Chanson, H., 2009. Turbulence measurements in positive surges and bores. Journal of Hydraulic Research, IAHR 47, 29–40. doi:10.3826/jhr.2009.2954.

Lubin, P., Chanson, H., Glockner, S., 2010. Large eddy simulation of turbulence generated by a weak breaking tidal bore. Environmental Fluid Mechanics 10, 587–602. doi:10.1007/s10652-009-9165-0.

Madsen, O.S., 1974. Stability of a sand bed under breaking waves. Proc. 13th Intl Conf. on Coastal Engineering, Copenhagen, Denmark, II, pp. 776–794.

Nielsen, P., 1992. Coastal bottom boundary layers and sediment transport. World Scientific, Advanced Series on Ocean Eng. 4, Singapore.

Nino, Y., Garcia, M.H., 1998. Using Lagrangian particle saltation observations for bedload sediment transport modelling. Hydrological Processes 12, 1197–1218.

Sumer, B.M., Oguz, B., 1978. Particle motions near the bottom in turbulent flow in an open channel. The Journal of Fluid Mechanics 78, 109–127.

Tessier, B., Terwindt, J.H.J., 1994. An example of soft-sediment deformations in an intertidal environment — the effect of a tidal bore. Comptes-Rendus de l'Académie des Sciences, Série II 319 (2), 217–233 (in French).

Tricker, R.A.R., 1965. Bores, breakers, waves and wakes. American Elsevier Publ. Co., New York, USA.